energies

MDPI

Article

Porous Activated Carbons Derived from Coffee Waste for Use as Functional Separators in Lithium-Sulfur Batteries

Jae-Hoon Shin †, Yu-Yeon Park †, Sang-Hyun Moon, Ji-Hwan Kim, Jae-Sung Jang, Sung-Beom Kim, Seong-Nam Lee and Kyung-Won Park *

Department of Chemical Engineering, Soongsil University, Seoul 06978, Korea
* Correspondence: kwpark@ssu.ac.kr; Tel.: +82-2-820-0613; Fax: +82-2-812-5378
† These authors contributed equally to this work.

Abstract: A novel approach has been proposed for improving the performance of lithium-sulfur batteries (LSBs) with a carbon-based material as an interlayer between the cathode and separator. With this method, the cross-over of lithium polysulfides (LiPS) to the anode is suppressed, increasing reutilization of the sulfur cathode. In this study, activated carbons (ACs) were prepared using coffee waste as a carbon source and potassium hydroxide (KOH) as an activation agent at various reaction temperatures ranging from 500 to 800 °C. With the rise in heating temperature, the specific surface areas, micro-surface areas, and micro-pore volumes of the AC samples gradually increased. In particular, the AC sample prepared at 800 °C and used as a functional separator for LSB exhibited improved capacity and cycling performance while suppressing the LiPS shuttle effect.

Keywords: lithium sulfur batteries; separator; coffee waste; activated carbon; shuttle effect; physical adsorption

Citation: Shin, J.-H.; Park, Y.-Y.; Moon, S.-H.; Kim, J.-H.; Jang, J.-S.; Kim, S.-B.; Lee, S.-N.; Park, K.-W. Porous Activated Carbons Derived from Coffee Waste for Use as Functional Separators in Lithium-Sulfur Batteries. *Energies* **2022**, *15*, 7961. https://doi.org/10.3390/en15217961

Academic Editor: Alvaro Caballero

Received: 27 September 2022
Accepted: 24 October 2022
Published: 27 October 2022

1. Introduction

Lithium-sulfur batteries (LSBs) are promising energy sources that can electrochemically convert chemical energy into electrochemical energy and vice versa because of their high theoretical capacity of 1675 mAh g^{-1}, high energy density of 2600 Wh kg^{-1}, and abundant resource of sulfur as an active material [1–3]. However, sulfur cathodes exhibit a low electrical conductivity of 5×10^{-30} S·cm^{-1} at 25 °C and high solubility in ether-based electrolytes [4,5]. Furthermore, LSBs have drawbacks such as electrical isolation of the sulfur cathode and dissolution of lithium polysulfides (LiPS) during the conversion process [6–8]. Problems associated with LSBs can lead to high polarization, low Coulombic efficiency, and rapid capacity decay [9–11]. In particular, LiPS (Li_2S_x ($4 \leq x \leq 8$), generated during charging/discharging, are highly soluble in electrolytes, thereby decreasing the number of active materials at the cathode [12–14]. Moreover, the dissolved LiPS are transported through the separator to the Li anode in the so-called "shuttle effect" of LiPS. The separator and Li anode may be covered by LiPS, producing insoluble Li_2S or Li_2S_2 insulating layers on the surface of the separator and anode, thereby deteriorating the LSB performance [15,16].

Thus, a novel approach has been proposed for improving the performance of LSBs with insertion of a carbon-based material as a functional separator between the cathode and separator. It suppresses the cross-over of LiPS to the anode and increases reutilization of the sulfur cathode [17,18]. Carbon-based functional separator materials, such as multi-walled carbon nanotubes and reduced graphene oxide, display the high electrical conductivity and improved physical adsorption properties of LiPS [19–22]. Furthermore, the physical adsorption ability of carbon-based materials, based on van der Waals forces, can block the diffusion of LiPS in the initial cycle. In general, carbons with micropores and mesopores provide high specific surface areas and facilitate Li^+ ion diffusion [23–25]. The specific

surface areas, micro surface areas, micropore volumes, and pore sizes of template carbons were compared with activated carbon (Table 1). In particular, carbon prepared using coffee waste has been utilized in various electrochemical applications [26–28]. Carbons derived from the coffee waste (Coffee extract, CAS 84650-00-0) have several advantages, such as eco-friendliness, low-cost, a well-defined porous structure, a fairly high surface area, and high electrical conductivity [29]. Shen et al. reported that the Li-S cell fabricated using activated carbon prepared from puffed corn showed enhanced electrochemical performance (787.6 mAh g^{-1}@0.5C) [30]. Furthermore, the carbon derived from coconut shell was applied to the Li-S cell and exhibited a high discharge capacity (846 mAh g^{-1}@0.5C) [31]. In this study, activated carbon (AC) samples were simply prepared using coffee waste as a carbon source and potassium hydroxide (KOH) as an activation agent at various reaction temperatures ranging from 500 to 800 °C. The AC samples exhibited amorphous crystals and well-formed porous structures with high specific surface areas. Specifically, the AC sample prepared at 800 °C was used as a functional separator material for LSBs and delivered the highest capacity and improved cycling performance because of its porous structure and high specific surface area.

Table 1. Comparison of specific surface areas, micro surface areas, micropore volumes, and pore sizes of the templated carbons and activated carbon determined from the N_2 isotherms.

Sample	BET Surface Area (m^2 g^{-1})	Micro Surface Area (m^2 g^{-1})	Micropore Volume (cm^3 g^{-1})	Median Pore Width (nm)	Ref.
Alumina-Sodium dodecyl sulfate	288	16	0.68	6.5	[32]
Zeolite	1664	597	1.0	1.3	[32]
Silica Gel	740	0	0.65	5.7	[32]
Activated carbon	1864	690	0.87	1.8	[31]

2. Experimental

2.1. Synthesis of Activated Carbons (ACs) Derived from Coffee Waste

Activated carbon (AC) was prepared using an activation process with coffee waste (Blended Milky Way, CAS 84650-00-0) and KOH (95%, SAMCHUN, Seoul, Korea) powder. Specifically, 2 g of coffee waste and 3 g of KOH flakes were mixed homogeneously in a mortar. The heat treatment was conducted with the mixed powder in an alumina tube at various temperatures ranging from 500 to 800 °C under N_2 gas atmosphere for 30 min. To remove impurities such as K and K_2CO_3, the heated samples were washed with 2 L deionized (DI) water and stirred in 2 M HCl solution for 12 h. The samples were completely washed with DI water to adjust the pH to 7.0 and dried in a vacuum oven at 50 °C for 12 h.

2.2. MWCNT/S as a Cathode

The MWCNT/S cathode for a functional separator was prepared using a multi-wall carbon nanotube (MWCNT, GRAPHENE SUPERMARKET, Ronkonkoma, NY, USA) and sulfur (S, 99.98%, Sigma Aldrich, St. Louis, MI, USA). For acid-treatment of MWCNT, 2 g of MWCNT powder was stirred in HCl (35%, 10 mL) and HNO_3 (60%, 30 mL) at 60 °C for 2 h. The acid-treated MWCNT was washed with DI water several times and dried in an oven at 50 °C for 12 h. The acid-treatment of MWCNT can increase the polarity of MWCNT and support the effective adsorption of MWCNT with polar polysulfides. MWCNT and sulfur were mixed with a weight ratio of 2:8 and ground. The mixture was transferred to a Teflon-lined autoclave and heated at 155 °C for 12 h.

2.3. Materials Characterization

The crystal structure was confirmed by X-ray diffraction (XRD, D2 PHASER, Bruker AXS, Madison, WI, USA) with Ni filter and Cu K_α X-ray source (λ = 0.154 nm). Raman spectroscopy (Leica DM2700 M, Leica Microsystems, Wetzlar, Germany) was performed

with a Nd:YAG laser (λ = 532 nm) in the waver number range of 800–2000 cm^{-1}. The shape and composition of the samples were observed using field emission scanning electron microscopy (FE-SEM, GeminiSEM 300, ZEISS, Oberkochen, Germany) and energy dispersive X-ray spectroscopy (EDX, XFlash Detector 6), respectively. The specific surface areas and pore structures of the samples were characterized using an N_2 adsorption/desorption analyzer (Micromeritics ASAP 2020) according to the BET (Brunauer–Emmett–Teller) theory and BJH (Barrett–Joyner–Halenda) method. The degassing temperature was 200 °C in air. The presence of impurities in the activated carbon samples was confirmed by thermal gravimetric analysis (TGA, TGA 2-XP1, METTLER TOLEDO, Columbus, OH, USA) in the temperature range from 25 to 800 °C under an air ambience. The Li_2S_6 adsorption capability of the samples was measured by UV/VIS spectroscopy (UV/VIS spectrophotometer, V-650, JASCO, Oklahoma City, OK, USA).

2.4. Electrochemical Measurements

To fabricate an functional separator structure for LSB, the AC sample was mixed at a weight ratio of 9:1 (AC:polyvinylidene fluoride (PVDF, Alfa Aesar, Ward Hill, MA, USA)) in N-methyl-2-pyrrolidone (NMP, Samchun). The paste was evenly applied on a polypropylene (PP, Celgard 2400) separator using a doctor blade method. The coated separator was dried in a vacuum oven at 50 °C for 12 h and cut to a diameter of 19 mm. The mass loading of the AC sample on the coated separator was 0.70 mg cm^{-2}. In addition, to fabricate the cathode for LSBs, MWCNT/S (80 wt%) as an active material was mixed homogeneously in NMP using a paste mixer with super P (10 wt%, Alfa Aesar) and PVDF (10 wt%) as the conducting agent and binder, respectively. The slurry was applied using the doctor blade method onto aluminum foil and then dried in a vacuum oven at 50 °C for 48 h. The dried foil was cut to a diameter of 13 mm. The load amount of sulfur was 2.0–2.1 mg cm^{-2}. Coin cells (size 2032, Hohsen Corporation, Osaka, Japan) for LSBs were assembled in an Ar-filled glove box with a sulfur cathode on aluminum-foil, a Li metal anode, and sample-coated polypropylene as a functional separator. The electrolyte was prepared by dissolving 1.0 M lithium bis(trifluoromethanesulfonyl)imide (LiTFSI, Aldrich) and 0.2 M $LiNO_3$ (Alfa Aesar) in a 1:1 volume ratio of 1,3-dioxolane (DOL, TCI chemical, Tokyo, Japan) and 1,2-dimethoxyethane (DME, TCI Chemical). The ratio of electrolyte to S was 15 μL mg^{-1}. Charge–discharge curves were obtained at a current density of 0.5 C with a battery tester (WBCS3000Le, WonATech Co. Ltd., Seoul, Korea) in 1.8–2.6 V vs. Li/Li^+.

3. Results and Discussion

In this study, we synthesized porous AC from coffee waste using the KOH activation mechanism as follows [33,34]:

$$\text{Coffee waste} + 2KOH \rightarrow \text{Coffee waste} + K_2O + H_2O \quad (1)$$

$$\text{Coffee waste} + H_2O \rightarrow \text{Char; C} + H_2O + \text{Tar} \quad (2)$$

$$C + H_2O \rightarrow H_2 + CO \quad (3)$$

$$C + 4KOH \rightarrow K_2O + 3H_2 + K_2CO_3\ (600\ ^\circ C) \quad (4)$$

$$K_2CO_3 \rightarrow K_2O + CO_2\ (700\ ^\circ C) \quad (5)$$

$$2C + K_2CO_3 \rightarrow 2K + 3CO\ (700\ ^\circ C) \quad (6)$$

$$C + K_2O \rightarrow 2K + CO\ (800\ ^\circ C) \quad (7)$$

Coffee waste was thermally decomposed into carbon through the physical activation process, i.e., carbonization (step (1)–(3)). In step (1), KOH is dehydrated into potassium oxide (K_2O) and water (H_2O), and the main components of coffee waste, such as cellulose, hemicellulose, and lignin, are distorted and cracked. In step (2) and (3), the pores are formed via the gas (tar or CO) emission. Lignocellulosic materials are aromatized into char through a thermal decomposition process at 450~500 °C (steps (1)–(3)). In step (4)–(7), the

additional thermal decomposition occurs, which corresponds to the chemical activation process, drastically increasing specific surface areas and pore volumes. In step (4), the interaction between KOH and carbon at 600 °C produces K_2O and potassium carbonate (K_2CO_3). Moreover, the K_2CO_3 formed in step (4) is partially decomposed into K_2O and carbon dioxide (CO_2) at ~700 °C (step (5)). At 700–800 °C, K_2O and K_2CO_3 formed in step (4) react with carbon to produce metallic potassium and carbon monoxide (CO) (steps (6) and (7)). Hence, according to the KOH activation mechanism, with increasing activation temperature, the physical (step (1)–(3)) and chemical (step (4)–(7)) activation processes can induce the increased specific surface area and pore size. At 500 °C, lignin, one of the main components of coffee waste, may be incompletely carbonized. Figure 1 shows SEM images of the samples prepared with coffee waste at different reaction temperatures ranging from 500 to 800 °C (AC-500, AC-600, AC-700, and AC-800). Specifically, it was found that a porous carbon structure could be formed via etching in steps (4) and (5) through (6) and (7). With increasing reaction temperatures, the KOH activation processes (steps (6) and (7)) could be improved, thus forming a more porous AC structure. The specific surface areas and pore structures of the AC samples are compared in Figure 2 and Table 2. The samples exhibited type-I N_2 isotherms, implying a microporous structure. As the reaction temperature increased from 500 to 800 °C, the specific surface areas, micro-surface area, and micro-pore volumes gradually increased. However, the samples prepared at 800 °C, at which the KOH etching process that occurred most actively, had the highest specific surface area (~1940 m^2 g^{-1}) and a significantly increased meso-surface area.

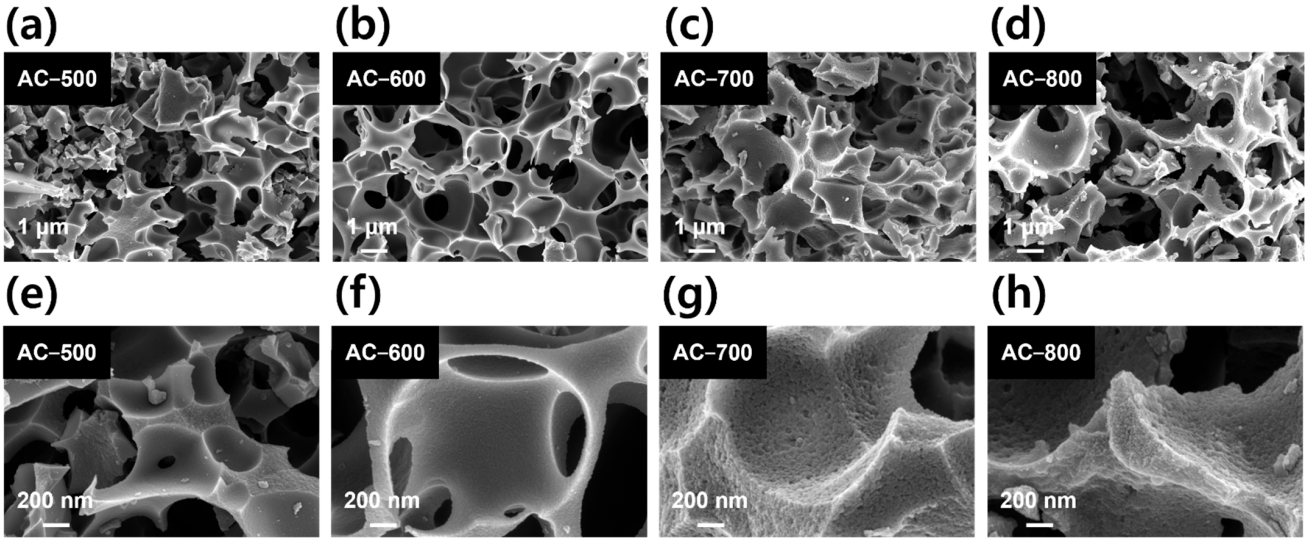

Figure 1. SEM images of the activated carbon (AC) samples prepared with coffee waste at different reaction temperatures from 500 to 800 °C. (**a**) AC-500; (**b**) AC-600; (**c**) AC-700; (**d**) AC-800 of low magnification SEM images; (**e**) AC-500; (**f**) AC-600 ; (**g**) AC-700; (**h**) AC-800 of high magnification SEM images.

Table 2. Comparison of specific surface areas and pore structures of the AC samples determined from the N_2 isotherms.

Sample	BET Surface Area (m^2 g^{-1})	Micro Surface Area (m^2 g^{-1})	Micropore Volume (cm^3 g^{-1})	Median Pore Width (nm)
AC-500	761 ± 11.89	629 ± 9.79	0.24 ± 0.005	0.54 ± 0.003
AC-600	1054 ± 17.42	938 ± 6.70	0.36 ± 0.006	0.51 ± 0.001
AC-700	1464 ± 25.26	1295 ± 12.54	0.49 ± 0.004	0.54 ± 0.001
AC-800	1940 ± 32.77	1470 ± 35.38	0.58 ± 0.02	0.61 ± 0.003

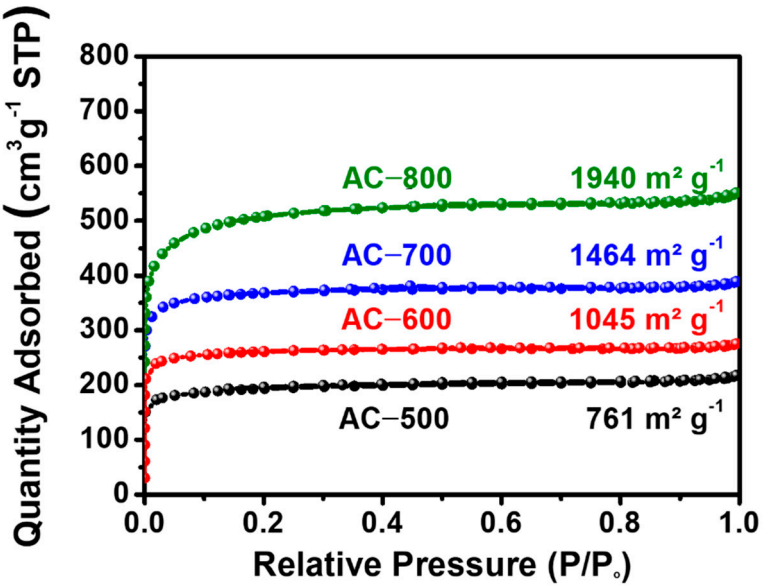

Figure 2. The N_2 isotherms of AC-500, AC-600, AC-700, and AC-800.

Figure 3 shows the XRD patterns of the AC-500, AC-600, AC-700, and AC-800 samples. In general, for the carbon crystal structure, the main peaks corresponding to the (002) and (101) planes appear at ~23.0° and ~43.5°, respectively [35]. All samples exhibited broad carbon peaks with lower angle shifts, compared to a typical carbon structure, without impurities (K_2O, K_2CO_3, and K) being generated during the thermal activation process. The broad peaks of the samples may result from pores or defects in the carbon structure caused by the KOH activation process [36–38]. It was reported that more nanoporous structures exhibited an increased intensity of XRD peaks at ~10° [39,40]. In this study, as reaction temperature increased, the samples became more nanoporous. Raman spectroscopy analysis was performed to further characterize the crystal structures of the samples (Figure 4a). All samples contained characteristic peaks corresponding to the D- and G-bands of the carbon structure, which are associated with defects and a graphitic structure, respectively, at ~1350 and ~1580 cm^{-1}, respectively [41]. Specifically, the broad peaks and high intensity ratios of the D- to G-bands (I_D/I_G) indicate that pure carbon structures without any other phases such as K_2O, K_2CO_3, and K could be formed by the KOH activation process with coffee waste. In addition, the I_D/I_G values of AC-500, AC-600, AC-700, and AC-800 were determined to be 0.84, 0.81, 0.92, and 0.87, respectively, indicating that AC samples are graphitic carbon materials. The presence of impurities in the samples was confirmed by the thermogravimetric analysis (TGA) in the temperature range of 25–800 °C in an air (Figure 4b). The evaporation of water molecules was observed from 25 to 150 °C with a weight loss of 8%. Overall, the single weight loss from 150 to 600 °C, indicative of oxidation of the pure carbon structure, demonstrates that the carbon structure with a single phase was formed without impurities and other phases.

Figure 5 shows the SEM-EDX mapping data of the AC-500, AC-600, AC-700, and AC-800 samples. The compositions of main elements corresponding to C, O, and N were 78–83%, 8–13%, and 6–8%, respectively. The impurities such as K_2O and K_2CO_3 were found to be completely removed out in the samples via leaching and washing processes. In addition, the presence of N indicates the formation of N-doped activated carbon through heat treatment under the N_2 atmosphere.

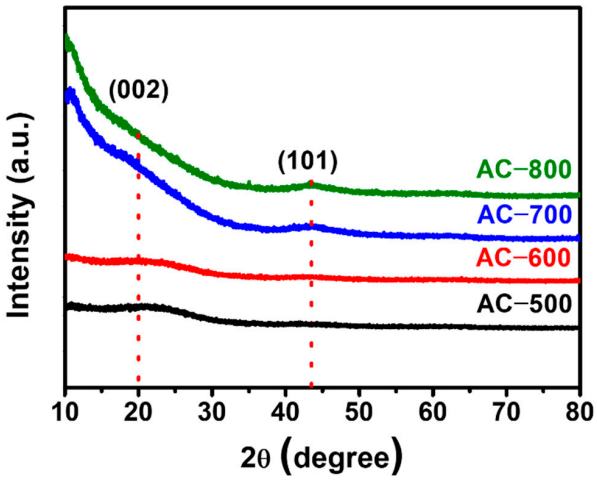

Figure 3. The XRD patterns of AC-500, AC-600, AC-700, and AC-800.

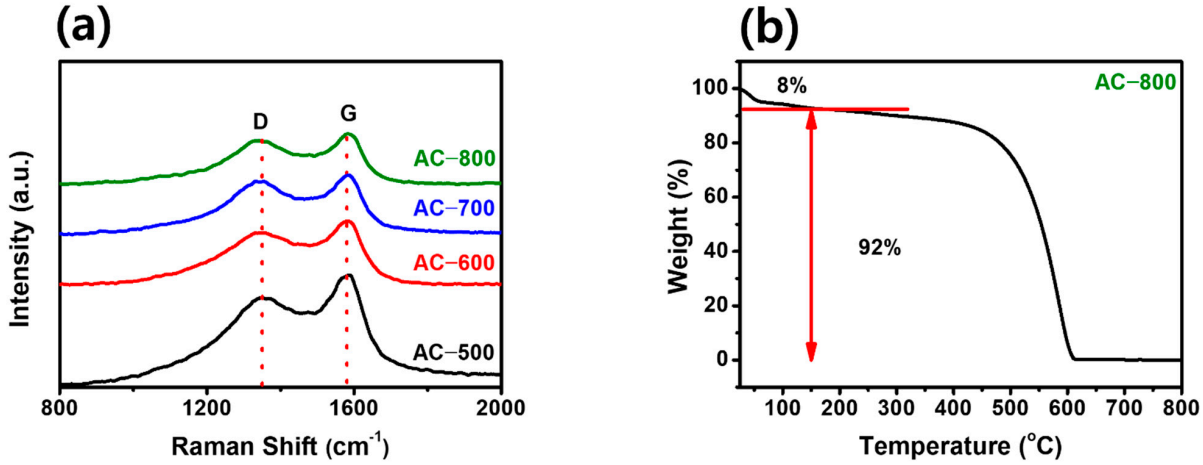

Figure 4. (**a**) Raman spectra (D- and G-bands represent defects and a graphitic structure, respectively.) and (**b**) TGA curves of the AC samples.

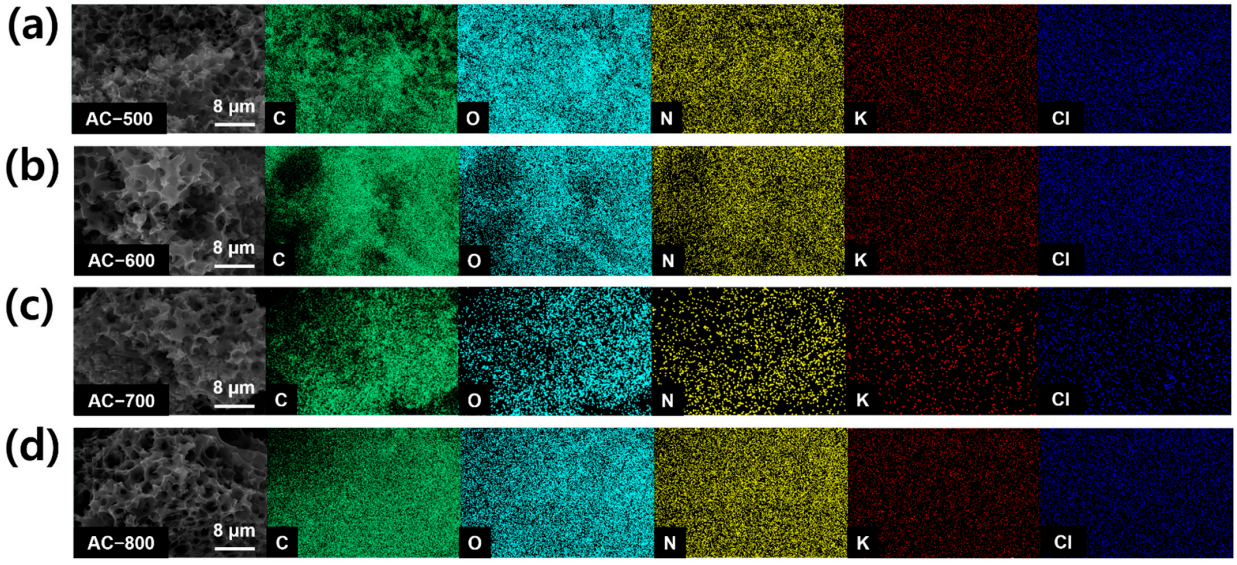

Figure 5. SEM-EDX mapping images of elements such as C, O, N, K, and Cl (**a**) AC-500, (**b**) AC-600, (**c**) AC-700, and (**d**) AC-800.

To characterize the LiPS adsorption capability of the samples, UV-vis spectroscopy tests were conducted (Figure 6). The samples (40 mg) were added to 50 mM Li_2S_6 solutions (50 mL) and stored at room temperature for 12 h. After the 12 h adsorption test, the UV-vis absorption spectra were measured in the wavelength range of 250–500 nm to investigate the concentration of Li_2S_6 remaining in the solutions. Typically, absorbance peaks corresponding to S_6^{2-} species are observed at 260, 280, 300, and 340 nm [42,43]. In this study, the order of the Li_2S_6 absorption peak intensity was AC-500 > AC-600 > AC-700 > AC-800, whereas the order of the adsorption capability of the samples was AC-800 > AC-700 > AC-600 > AC-500. Hence, the AC-800, which has the highest specific surface area and a significantly increased meso-surface area, exhibited the best LiPS adsorption properties, which could block the migration of LiPS [44].

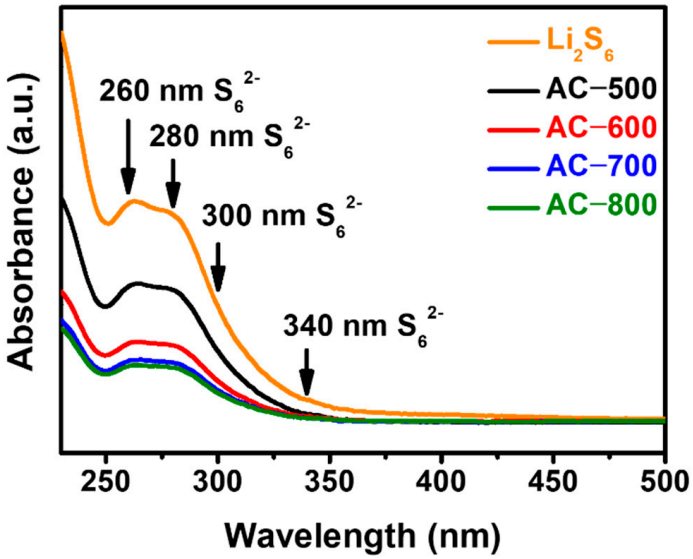

Figure 6. UV-vis absorbance spectra of the AC samples as the functional separators.

Figure 7 shows CVs of the assembled coin cells with the AC functional separators (0.70 mg cm^{-2} of the AC sample) and MWCNT/S cathode (2.0–2.1 mg cm^{-2}) measured in the potential range of 1.8–2.6 V vs Li/Li^+ at a scan rate of 0.01 mV s^{-1}. All the AC samples exhibited characteristic peaks corresponding to reduction reactions and oxidation reactions of solid S_8 to polysulfide Li_2S_x ($1 \leq n \leq 8$). During discharging, the 1st reduction peaks were observed at 2.28–2.30 V, transforming solid S_8 to soluble polysulfide ($4 \leq x \leq 8$), and the 2nd reduction peaks were observed at 2.05–2.07 V, transforming soluble polysulfide ($4 \leq x \leq 8$) to insoluble Li_2S_x ($1 \leq x \leq 2$). During charging, two distinct oxidation peaks were observed at 2.29–2.32 and 2.37–2.40 V, respectively, transforming insoluble Li_2S_2/Li_2S to ring-type S_8 [45]. However, with the rise in heating temperature, the peak areas associated with electrochemical reactions of LiPS gradually increased. As previously mentioned, as the heating temperature increased from 500 to 800 °C, the specific surface areas, micro-surface areas, and micro-pore volumes gradually increased. The AC-800 with the highest specific surface area and meso-surface area exhibited the largest CV area, which could result from the electrochemical response of LiPS adsorbed in the porous carbon structure [46].

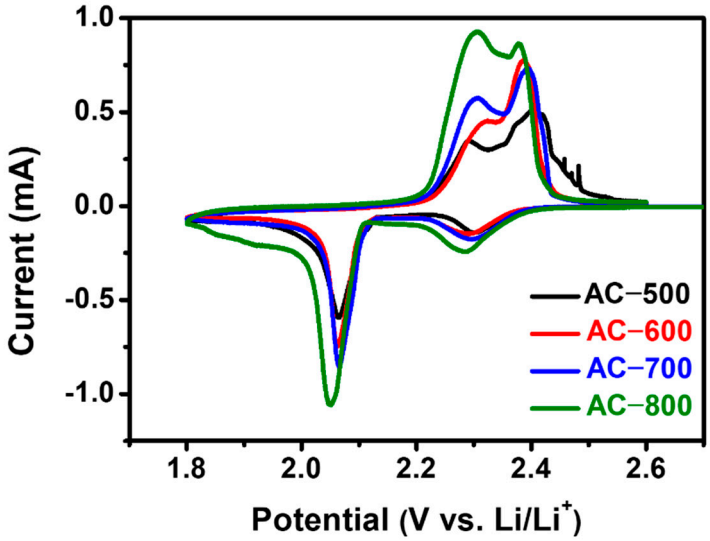

Figure 7. CVs of the AC samples measured in the potential range of 1.8–2.6 V vs Li/Li^+ at a scan rate of 0.01 mV s^{-1}.

Characteristic charge-discharge curves of the Li/S cells with the AC samples as functional separators and a pristine PP separator were measured at a current density of 0.1 C in the potential range of 1.8–2.6 V vs Li/Li^+ (Figure 8a). All cells have two plateaus at 2.2–2.4 and 2.0–2.1 V, observed during discharging [47]. The first plateau represents the electrochemical reduction of solid-state S_8 to long chain polysulfide ($4 \leq x \leq 8$), corresponding to 25% of the theoretical capacity of sulfur. In the 2nd plateau, long-chain polysulfide ($4 \leq x \leq 8$) is electrochemically reduced to short chain polysulfide (Li_2S_x ($1 \leq x \leq 2$)), contributing to 75% of the theoretical capacity of sulfur [48,49]. On the contrary, during charging, Li_2S_2 and Li_2S in the first plateau are oxidized to soluble long-chain polysulfide ($4 \leq x \leq 8$) and soluble long-chain polysulfides ($4 \leq x \leq 8$) in the 2nd plateau are oxidized to solid-state S_8, which are identical to oxidation- and reduction-related peaks in the CVs [50,51]. The initial discharge capacities of the Li/S cells with PP, AC-500, AC-600, AC-700, and AC-800 were 738, 897, 944, 977, and 992 mAh g^{-1}, respectively. Compared to the PP separator, the high electrical conductivity of the AC samples as the functional separators can lead to high capacities and improved redox reaction rates [52]. In particular, the porous structure of the AC samples can facilitate Li^+ ion transport and increase the reaction sites, thereby enhancing the electrochemical performance [53]. The capacity of the Li/S cells increased with increasing heating temperature. The increased electrochemical reaction corresponding to LiPS adsorbed in the porous carbon structures may be attributed to the increased specific surface areas, micro-surface areas, and micro-pore volumes with increasing heating temperature [54]. Hence, AC-800 with the highest specific surface area and meso-surface area exhibited the highest discharge capacity. Figure 8b shows the cycling performance of the Li/S cells measured at 0.1 C for 100 cycles. The discharge capacities of the Li/S cells with AC-500, AC-600, AC-700, and AC-800 measured at 100 cycles were 610, 645, 698, and 767mAh g^{-1}, respectively. The retentions of the Li/S cells with AC-500, AC-600, AC-700, and AC-800 measured at 100 cycles were 68%, 68%, 71%, and 77%, respectively. All the Li/S cells exhibited ~100% Coulombic efficiency. The cycling performance of the Li/S cells was recorded at a higher current density of 0.5 C for 100 cycles (Figure 8c). The first discharge capacities of the Li/S cells with PP separator, AC-500, AC-600, AC-700, and AC-800 were 252, 649, 670, 673, and 719 mAh g^{-1}, respectively. The retentions of the Li/S cells with AC-500, AC-600, AC-700, and AC-800 as the functional separators after 100 cycles were 63%, 81%, 88%, and 92%, respectively. As a result, AC-800, with an improved porous structure significantly maintained the electrochemical reaction of LiPS, thus suppressing the LiPS shuttle effect.

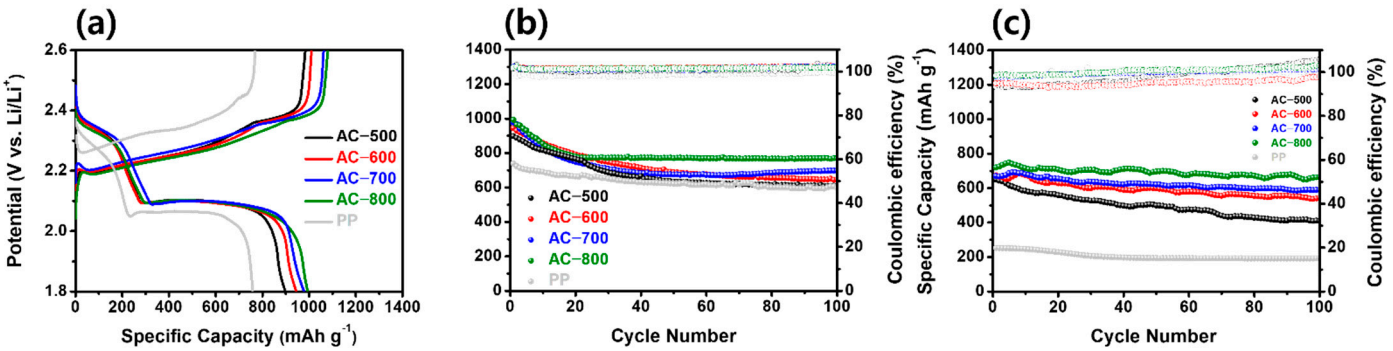

Figure 8. (**a**) Characteristic charge-discharge curves of the Li/S cells with AC samples as functional separators and a pristine PP separator measured at a current density of 0.1 C of the first cycle in the potential range of 1.8–2.6 V vs. Li/Li^+. (**b**) Cycling performance of the Li/S cells recorded at a current density of 0.1 C for 100 cycles (The transparent dots are Coulombic efficiencies of the samples). (**c**) Cycling performance of the Li/S cells recorded at a current density of 0.5 C for 100 cycles.

4. Conclusions

In summary, the AC samples were prepared using coffee waste as the carbon source and KOH as the activation agent at various reaction temperatures. The AC samples exhibited amorphous crystals and well-defined porous structures with high specific surface areas. With increasing heating temperature, the specific surface areas, micro-surface areas, and micro-pore volumes of the AC samples gradually increased. In particular, the AC sample prepared at 800 °C and used as a functional separator material for LSB exhibited the highest capacity and improved cycling performance, thereby suppressing the LiPS shuttle effect because of its improved porous structure.

Author Contributions: J.-H.S.: Conceptualization, Methodology, Formal analysis. Y.-Y.P.: Formal analysis, Data curation, Writing—original draft. S.-H.M.: Investigation, Data curation. J.-H.K.: Data curation. J.-S.J.: Data curation. S.-B.K.: Data curation. S.-N.L.: Data curation. K.-W.P.: Conceptualization, Supervision, Writing—review & editing. All authors have read and agreed to the published version of the manuscript.

Funding: This research was supported by the National Research Foundation of Korea (2020R1A2C2010510, 2020R1A6A1A03044977).

Data Availability Statement: The data can be shared up on request.

Conflicts of Interest: The authors declare no conflict of interest.

References

1. Tao, T.; Lu, S.; Fan, Y.; Lei, W.; Huang, S.; Chen, Y. Anode Improvement in Rechargeable Lithium–Sulfur Batteries. *Adv. Mater.* **2017**, *29*, 1700542. [CrossRef] [PubMed]
2. Ren, W.; Ma, W.; Zhang, S.; Tang, B. Recent advances in shuttle effect inhibition for lithium sulfur batteries. *Energy Storage Mater.* **2019**, *23*, 707–732. [CrossRef]
3. Li, J.; Wei, W.; Meng, L. Liquid-phase exfoliated-graphene-supporting nanostructural sulfur as high-performance lithium–sulfur batteries cathode. *Compos. Commun.* **2019**, *15*, 149–154. [CrossRef]
4. Sun, J.; Ma, J.; Fan, J.; Pyun, J.; Geng, J. Rational design of sulfur-containing composites for high-performance lithium-sulfur batteries. *APL Mater.* **2019**, *7*, 020904. [CrossRef]
5. Pan, Z.; Brett, D.J.L.; He, G.; Parkin, I.P. Progress and Perspectives of Organosulfur for Lithium–Sulfur Batteries. *Adv. Energy Mater.* **2022**, *12*, 2103483. [CrossRef]
6. Zhu, J.; Zou, J.; Cheng, H.; Gu, Y.; Lu, Z. High energy batteries based on sulfur cathode. *Green Energy Environ.* **2019**, *4*, 345–359. [CrossRef]
7. Sadd, M.; De Angelis, S.; Colding-Jørgensen, S.; Blanchard, D.; Johnsen, R.E.; Sanna, S.; Borisova, E.; Matic, A.; Bowen, J.R. Visualization of Dissolution-Precipitation Processes in Lithium–Sulfur Batteries. *Adv. Energy Mater.* **2022**, *12*, 2103126. [CrossRef]
8. Yu, L.; Ong, S.J.H.; Liu, X.; Mandler, D.; Xu, Z.J. The importance of the dissolution of polysulfides in lithium-sulfur batteries and a perspective on high-energy electrolyte/cathode design. *Electrochim. Acta* **2021**, *392*, 139013. [CrossRef]

9. Zhao, M.; Li, B.Q.; Zhang, X.Q.; Huang, J.Q.; Zhang, Q. A Perspective toward Practical Lithium-Sulfur Batteries. *ACS Cent. Sci.* **2020**, *6*, 1095–1104. [CrossRef]
10. Zhao, Z.; Pathak, R.; Wang, X.; Yang, Z.; Li, H.; Qiao, Q. Sulfiphilic FeP/rGO as a highly efficient sulfur host for propelling redox kinetics toward stable lithium-sulfur battery. *Electrochim. Acta* **2020**, *364*, 137117. [CrossRef]
11. Li, S.; Zhang, W.; Zheng, J.; Lv, M.; Song, H.; Du, L. Inhibition of Polysulfide Shuttles in Li–S Batteries: Modified Separators and Solid-State Electrolytes. *Adv. Energy Mater.* **2021**, *11*, 2000779. [CrossRef]
12. Shen, C.; Xie, J.; Zhang, M.; Andrei, P.; Zheng, J.P.; Hendrickson, M.; Plichta, E.J. A Li-Li_2S_4 battery with improved discharge capacity and cycle life at low electrolyte/sulfur ratios. *J. Power Sources* **2019**, *414*, 412–419. [CrossRef]
13. Li, S.; Leng, D.; Li, W.; Qie, L.; Dong, Z.; Cheng, Z.; Fan, Z. Recent progress in developing Li_2S cathodes for Li–S batteries. *Energy Storage Mater.* **2020**, *27*, 279–296. [CrossRef]
14. Zhang, J.; Li, M.; Younus, H.A.; Wang, B.; Weng, Q.; Zhang, Y.; Zhang, S. An overview of the characteristics of advanced binders for high-performance Li–S batteries. *Nano Mater. Sci. J.* **2021**, *3*, 124–139. [CrossRef]
15. Deng, S.; Yan, Y.; Wei, L.; Li, T.; Su, X.; Yang, X.; Li, Z.; Wu, M. Amorphous Al_2O_3 with N-Doped Porous Carbon as Efficient Polysulfide Barrier in Li−S Batteries. *ACS Appl. Energy Mater.* **2019**, *2*, 1266–1273. [CrossRef]
16. Kim, S.; Lim, W.G.; Cho, A.; Jeong, J.; Jo, C.; Kang, D.; Han, S.M.; Han, J.W.; Lee, J. Simultaneous Suppression of Shuttle Effect and Lithium Dendrite Growth by Lightweight Bifunctional Separator for Li-S Batteries. *ACS Appl. Energy Mater.* **2020**, *3*, 2643–2652. [CrossRef]
17. Fan, L.; Li, M.; Li, X.; Xiao, W.; Chen, Z.; Lu, J. Interlayer Material Selection for Lithium-Sulfur Batteries. *Joule* **2019**, *3*, 361–386. [CrossRef]
18. Chen, L.; Yu, H.; Li, W.; Dirican, M.; Liu, Y.; Zhang, X. Interlayer design based on carbon materials for lithium-sulfur batteries: A review. *J. Mater. Chem. A* **2020**, *8*, 10709–10735. [CrossRef]
19. Wei, H.; Liu, Y.; Zhai, X.; Wang, F.; Ren, X.; Tao, F.; Li, T.; Wang, G.; Ren, F. Application of Carbon Nanotube-Based Materials as Interlayers in High-Performance Lithium-Sulfur Batteries: A Review. *Front. Energy Res.* **2020**, *8*, 585795. [CrossRef]
20. Li, M.; Fu, K.; Wang, Z.; Cao, C.; Yang, J.; Zhai, Q.; Zhou, Z.; Ji, J.; Xue, Y.; Tang, C. Enhanced Adsorption of Polysulfides on Carbon Nanotubes/Boron Nitride Fibers for High-Performance Lithium-Sulfur Batteries. *Chem. A Eur. J.* **2020**, *26*, 17567–17573. [CrossRef]
21. Xu, T.; Song, J.; Gordin, M.L.; Sohn, H.; Yu, Z.; Chen, S.; Wang, D. Mesoporous Carbon–Carbon Nanotube–Sulfur Composite Microspheres for High-Areal-Capacity Lithium–Sulfur Battery Cathodes. *ACS Appl. Mater. Interfaces* **2013**, *5*, 11355–11362. [CrossRef] [PubMed]
22. Petnikota, S.; Rotte, N.K.; Srikanth, V.V.S.S.; Kota, B.S.R.; Reddy, M.V.; Loh, K.P.; Chowdari, B.V.R. Electrochemical studies of few-layered graphene as an anode material for Li ion batteries. *J. Solid State Electrochem.* **2014**, *18*, 941–949. [CrossRef]
23. Suleman, M.; Othman, M.A.R.; Hashmi, S.A.; Kumar, Y.; Deraman, M.; Omar, R.; Jasni, M.R.M. Activated graphene oxide/reduced graphene oxide electrodes and low viscous sulfonium cation based ionic liquid incorporated flexible gel polymer electrolyte for high rate supercapacitors. *J. Alloys Compd.* **2017**, *695*, 3376–3392. [CrossRef]
24. Tsai, W.Y.; Lin, R.; Murali, S.; Li Zhang, L.; McDonough, J.K.; Ruoff, R.S.; Taberna, P.L.; Gogotsi, Y.; Simon, P. Outstanding performance of activated graphene based supercapacitors in ionic liquid electrolyte from −50 to 80 °C. *Nano Energy* **2013**, *2*, 403–411. [CrossRef]
25. Nishihara, H.; Kyotani, T. Zeolite-templated carbons—Three-dimensional microporous graphene frameworks. *Chem. Commun.* **2018**, *54*, 5648. [CrossRef]
26. Chung, D.Y.; Son, Y.J.; Yoo, J.M.; Kang, J.S.; Ahn, C.Y.; Park, S.; Sung, Y.E. Coffee Waste-Derived Hierarchical Porous Carbon as a Highly Active and Durable Electrocatalyst for Electrochemical Energy Applications. *ACS Appl. Mater. Interfaces* **2017**, *9*, 41303–41313. [CrossRef]
27. Zhao, P.; Shiraz, M.H.A.; Zhu, H.; Liu, Y.; Tao, L.; Liu, J. Hierarchically porous carbon from waste coffee grounds for high-performance Li–Se batteries. *Electrochim. Acta* **2019**, *325*, 134931. [CrossRef]
28. Sangprasert, T.; Sattayarut, V.; Rajrujithong, C.; Khanchaitit, P.; Khemthong, P.; Chanthad, C.; Grisdanurak, N. Making use of the inherent nitrogen content of spent coffee grounds to create nanostructured activated carbon for supercapacitor and lithium-ion battery applications. *Diam. Relat. Mater.* **2022**, *127*, 109164. [CrossRef]
29. Colon, M.; Nerin, C. Role of catechins in the antioxidant capacity of an active film containing green tea, green coffee, and grapefruit extracts. *J. Agric. Food Chem.* **2012**, *60*, 9842–9849. [CrossRef]
30. Zhu, L.; Jiang, H.; Yang, Q.; Yao, S.; Shen, X.; Tu, F. An Effective Porous Activated Carbon Derived from Puffed Corn Employed as the Separator Coating in a Lithium–Sulfur Battery. *Energy Technol.* **2019**, *7*, 1900752. [CrossRef]
31. Manoj, M.; Muhamed Ashraf, C.; Jasna, M.; Anilkumar, K.M.; Jinisha, B.; Pradeep, V.S.; Jayalekshmi, S. Biomass-derived, activated carbon-sulfur composite cathode with a bifunctional interlayer of functionalized carbon nanotubes for lithium-sulfur cells. *J. Colloid Interface Sci.* **2019**, *535*, 287–299. [CrossRef] [PubMed]
32. Singh, S.B.; De, M. Alumina based doped templated carbons: A comparative study with zeolite and silica gel templates. *Microporous Mesoporous Mater.* **2018**, *257*, 241–252. [CrossRef]
33. El-Hendawy, A.N.A. An insight into the KOH activation mechanism through the production of microporous activated carbon for the removal of Pb^{2+} cations. *Appl. Surf. Sci.* **2009**, *255*, 3723–3730. [CrossRef]

34. Xia, C.; Shi, S.Q. Self-activation for activated carbon from biomass: Theory and parameters. *Green Chem.* **2016**, *18*, 2063–2071. [CrossRef]
35. Shiryaev, A.A.; Voloshchuk, A.M.; Volkov, V.V.; Averin, A.A.; Artamonova, S.D. Nanoporous active carbons at ambient conditions: A comparative study using X-ray scattering and diffraction, Raman spectroscopy and N_2 adsorption. *J. Phys. Conf. Ser.* **2017**, *848*, 012009. [CrossRef]
36. Bai, L.; Ge, Y.; Bai, L. Boron and nitrogen co-doped porous carbons synthesized from polybenzoxazines for high-performance supercapacitors. *Coatings* **2019**, *9*, 657. [CrossRef]
37. Ma, F.; Ding, S.; Ren, H.; Liu, Y. Sakura-based activated carbon preparation and its performance in supercapacitor applications. *RSC Adv.* **2019**, *9*, 2474–2483. [CrossRef]
38. de Paula, F.G.F.; Campello-Gómez, I.; Ortega, P.F.R.; Rodríguez-Reinoso, F.; Martínez-Escandell, M.; Silvestre-Albero, J. Structural flexibility in activated carbon materials prepared under harsh activation conditions. *Materials* **2019**, *12*, 1988. [CrossRef]
39. Zhu, Y.; Murali, S.; Stoller, M.D.; Ganesh, K.J.; Cai, W.; Ferreira, P.J.; Pirkle, A.; Wallace, R.M.; Cychosz, K.A.; Thommes, M.; et al. Carbon-Based Supercapacitors Produced by Activation of Graphene. *Science* **2011**, *332*, 1537–1541. [CrossRef]
40. Men'Shchikov, I.; Shkolin, A.; Khozina, E.; Fomkin, A. Thermodynamics of adsorbed methane storage systems based on peat-derived activated carbons. *Nanomaterials* **2020**, *10*, 1379. [CrossRef]
41. Shrestha, R.L.; Chaudhary, R.; Shrestha, T.; Tamrakar, B.M.; Shrestha, R.G.; Maji, S.; Hill, J.P.; Ariga, K.; Shrestha, L.K. Nanoarchitectonics of Lotus Seed Derived Nanoporous Carbon Materials for Supercapacitor Applications. *Materials* **2020**, *13*, 5434. [CrossRef] [PubMed]
42. He, J.; Chen, Y.; Manthiram, A. MOF-derived Cobalt Sulfide Grown on 3D Graphene Foam as an Efficient Sulfur Host for Long-Life Lithium-Sulfur Batteries. *iScience* **2018**, *4*, 36–43. [CrossRef] [PubMed]
43. Li, W.; Qian, J.; Zhao, T.; Ye, Y.; Xing, Y.; Huang, Y.; Wei, L.; Zhang, N.; Chen, N.; Li, L.; et al. Boosting High-Rate Li–S Batteries by an MOF-Derived Catalytic Electrode with a Layer-by-Layer Structure. *Adv. Sci.* **2019**, *6*, 1802362. [CrossRef] [PubMed]
44. Mahankali, K.; Nagarajan, S.; Thangavel, N.K.; Rajendran, S.; Yeddala, M.; Arava, L.M.R. Metal-Based Electrocatalysts for High-Performance Lithium-Sulfur Batteries: A Review. *Catalysts* **2020**, *10*, 1137. [CrossRef]
45. Huang, X.; Wang, Z.; Knibbe, R.; Luo, B.; Abdul Ahad, S.; Sun, D.; Wang, L. Cyclic Voltammetry in Lithium–Sulfur Batteries—Challenges and Opportunities. *Energy Technol.* **2019**, *7*, 1801001. [CrossRef]
46. Wang, R.; Wu, R.; Ding, C.; Chen, Z.; Xu, H.; Liu, Y.; Zhang, J.; Ha, Y.; Fei, B.; Pan, H. Porous Carbon Architecture Assembled by Cross-Linked Carbon Leaves with Implanted Atomic Cobalt for High-Performance Li–S Batteries. *Nano-Micro Lett.* **2021**, *13*, 151. [CrossRef]
47. Li, R.; Sun, X.; Zou, J.; He, Q. Coordination effect of biocatalyst dithiothreitol and aramid fiber interlayer for lithium-sulfur batteries. *J. Mater. Sci. Mater. Electron.* **2020**, *31*, 14233–14240. [CrossRef]
48. Wang, J.; Yang, J.; Wan, C.; Du, K.; Xie, J.; Xu, N. Sulfur Composite Cathode Materials for Rechargeable Lithium Batteries. *Adv. Funct. Mater.* **2003**, *13*, 487–492. [CrossRef]
49. Guo, J.; Liu, J. A binder-free electrode architecture design for lithium-sulfur batteries: A review. *Nanoscale Adv.* **2019**, *1*, 2104–2122. [CrossRef]
50. Yan, J.; Liu, X.; Li, B. Capacity Fade Analysis of Sulfur Cathodes in Lithium–Sulfur Batteries. *Adv. Sci.* **2016**, *3*, 1600101. [CrossRef]
51. Li, B.; Xie, M.; Yi, G.; Zhang, C. Biomass-derived activated carbon/sulfur composites as cathode electrodes for Li–S batteries by reducing the oxygen content. *RSC Adv.* **2020**, *10*, 2823–2829. [CrossRef] [PubMed]
52. Yang, W.; Yang, W.; Dong, L.; Gao, X.; Wang, G.; Shao, G. Enabling immobilization and conversion of polysulfides through a nitrogen-doped carbon nanotubes/ultrathin MoS_2 nanosheet core-shell architecture for lithium-sulfur batteries. *J. Mater. Chem. A* **2019**, *7*, 13103–13112. [CrossRef]
53. Wu, H.; Xia, L.; Ren, J.; Zheng, Q.; Xu, C.; Lin, D. A high-efficiency N/P co-doped graphene/CNT@porous carbon hybrid matrix as a cathode host for high performance lithium-sulfur batteries. *J. Mater. Chem. A* **2017**, *5*, 20458–20472. [CrossRef]
54. Qi, Y.; Li, Q.J.; Wu, Y.; Bao, S.J.; Li, C.; Chen, Y.; Wang, G.; Xu, M. A Fe_3N/carbon composite electrocatalyst for effective polysulfides regulation in room-temperature Na-S batteries. *Nat. Commun.* **2021**, *12*, 3791. [CrossRef] [PubMed]